OPEN ACCESS
IOP Publishing
Journal of Physics: Condensed Matter
J. Phys.: Condens. Matter **37** (2025) 235001 (11pp)
https://doi.org/10.1088/1361-648X/add6fe

Thermally-induced covalent coupling of cobalt porphyrin molecules on Au(111)

Mehdi Bouatou[1], Nicolás Montenegro-Pohlhammer[2], Rocío Sánchez-de-Armas[2], Carl Barthel[1], Carmen J Calzado[2] and Manuel Gruber[1,*]

[1] Faculty of Physics and CENIDE, University of Duisburg–Essen, 47057 Duisburg, Germany
[2] Departamento de Química Física, Universidad de Sevilla, c/ Profesor García González, s/n., 41012 Sevilla, Spain

E-mail: manuel.gruber@uni-due.de

Received 27 February 2025, revised 30 April 2025
Accepted for publication 9 May 2025
Published 20 May 2025

Abstract

We investigated the thermally induced covalent coupling of cobalt porphyrin (CoP) molecules on an Au(111) surface using scanning tunnelling microscopy and first-principle calculations. While CoP molecules deposited at room temperature remain isolated due to electrostatic repulsion, annealing the substrate leads to their aggregation into chain-like structures with covalent bonding. Three distinct bonding motifs are identified, with calculations revealing weak magnetic coupling between the $S = 1/2$ Co ions. This work evidences a straightforward method for synthesising multinuclear complexes with magnetically coupled spins on surfaces, offering potential applications in molecular spintronics.

Keywords: scanning tunnelling microscopy, homocoupling, self-assembly, porphyrin

1. Introduction

Molecular self-assembly on surfaces typically relies on van der Waals interactions between molecules [1, 2]. However, the formation of covalent bonds between neighboring molecules leads to increased intermolecular electronic coupling, which is in turn useful for transport across molecules and for intermolecular coupling of magnetic moments. Such properties are particularly relevant for the fields of molecular electronics and molecular spintronics [3, 4]. Surface-assisted molecular reactions have been extensively used to create networks of covalently bonded molecules [5–8]. These reactions are based on the combination of appropriate molecular precursors [9], surface properties [10], and external stimuli such as temperature [11–13] or voltage pulses [14, 15], which together facilitate the formation of covalent bonds between molecules on the supporting surface. Some control over the reaction, for instance steering the selectivity via adsorption of CO molecules, has also been reported [16]. Metalloporphyrins represent a prominent class of molecules [17] where thermally driven reactions on surfaces have been successfully utilized to achieve covalent coupling [18–20]. This process is often facilitated by substituting the porphyrins with specific peripheral functional groups that react to form covalent C–C bonds when the surface is annealed to an appropriate temperature. However, the substitution process can be complex and frequently requires multiple synthesis steps, either for the precursor molecules or for the covalent network formation on the surface. Conversely, porphyrin molecules on surfaces were shown to undergo covalent linking, at the so-called β and *meso* substitution sites (figure 1(A)), upon annealing without requiring peripheral substitution [21–24]. This simplifies the process and highlights the intrinsic reactivity of porphyrin as a promising alternative for on-surface covalent coupling strategies. This strategy has so far only been reported for *metal-free* and Zn porphyrin complexes.

* Author to whom any correspondence should be addressed.

Separately, there has been different strategies to couple the magnetic centers of molecules, ranging from the synthesis of three- [25, 26] and two-dimensional multinuclear complexes [27–29], the engineering of the molecular stacking of planar complexes [30–32], the surface-assisted covalent coupling relying on the Ullmann coupling [33, 34], and on the co-deposition of ligands and metal centers [35]. In particular, coupled spins in on-surface-synthesized graphene nanoribbons [36–38] and organic oligomers [39] have attracted significant interest in recent years. The homocoupling of magnetic porphyrin complexes represents an attractive alternative approach to couple molecular spins.

Following the observation of surface-assisted homocoupling of porphyrin molecules, i.e. the covalent coupling between identical molecules, we investigate the homocoupling of cobalt porphyrin (CoP) complexes adsorbed on a Au(111) surface using low-temperature scanning tunneling microscopy (STM) and density functional theory (DFT) calculations. Upon deposition of CoP on the sample held at room temperature, the adsorbed molecules remain isolated, in the form of monomers. Annealing of the sample leads to the formation of dendrite-like chains of CoP complexes, composed of covalently bonded molecules with bonds at different peripheral substitution sites of the porphyrin. The structures of dimers (different configurations) from gas-phase and on-surface DFT calculations laterally matches the size of the resolved topographic structures. The exchange coupling between Co ions in neighbouring, covalently bonded complexes was calculated to be approximately 1 meV, which is below the detection limit of our instrumentation. Nevertheless, this homocoupling strategy for achieving magnetic coupling between molecular spins holds significant promise for molecular spintronics [3, 4], as larger magnetic interactions are anticipated with other metal centres.

2. Methods

2.1. STM

The Au(111) surface was prepared via repeated cycles of Ar-ion sputtering and annealing at 500° C. STM tips were fabricated by electrochemical etching of tungsten wire in a NaOH solution and subsequently conditioned by sputtering with Neon (partial pressure of 5×10^{-7} mbar). The tips were further shaped *in situ* by gently indenting them into the Au(111) substrate, thereby coating them with gold. CoP molecules, purchased from Frontier Scientific and specified with a purity better than 94%, were sublimated under ultrahigh vacuum at 210 °C using an Knudsen cell. The sample was held at room temperature during deposition. STM measurements were conducted with a custom-built, variable-temperature scanning tunneling microscope, operated in ultrahigh vacuum at 10 K. All STM images were acquired in the constant-current mode. Differential-conductance was obtained by adding a modulation to the sample voltage (20 mV at 800 Hz) and extracting the corresponding induced current using a lock-in amplifier. This modulation voltage, while introducing additional broadening of the spectral features, enables faster data acquisition and thus helps minimize creep-related issues.

2.2. First-principle calculations

2.2.1. Gas-phase. The geometry of each molecule was optimized on the frame of the DFT approach, with Perdew–Burke–Ernzerhof (PBE) functional, the D3 Grimme dispersion correction [40], and def2tzvp basis set for all atoms. Once optimized, the frequencies of the normal vibration modes were calculated. All the calculations were performed with the ORCA 5.0.3 package [41].

2.2.2. Gibbs free energy. The enthalpy and entropy variation associated to the formation reaction of motifs A, B, and C (figure 5) $2\,\mathrm{CoP} \rightarrow \mathrm{motif}\,X + n\mathrm{H_2}$, with $n = 3$ for $X = \mathrm{A}$, and $n = 2$ for $X = \mathrm{B}$, C can be separated in different contributions as follows:

$$\begin{aligned}\Delta H(T) = \Delta E_{\mathrm{elec}} + \Delta \mathrm{ZPE} + \Delta H_{\mathrm{vib}}(T) \\ + \Delta H_{\mathrm{rot}}(T) + \Delta H_{\mathrm{trans}}(T)\end{aligned} \quad (1)$$

$$\Delta S(T) = \Delta S_{\mathrm{elec}} + \Delta S_{\mathrm{vib}}(T) + \Delta S_{\mathrm{rot}}(T) + \Delta S_{\mathrm{trans}}(T) \quad (2)$$

where ΔE_{elec} (ΔS_{elec}) corresponds to the difference of the computed electronic structure energy (entropy), ΔZPE is the difference between their zero-point vibrational energy, and ΔH_{vib} (ΔS_{vib}), ΔH_{rot} (ΔS_{rot}) and $\Delta H_{\mathrm{trans}}$ ($\Delta S_{\mathrm{trans}}$) are the vibrational, rotational and translational thermal contributions to the transition enthalpy (entropy). The electronic contribution to the enthalpy is zero, since there are no thermally accessible electronic excited states. All the contributions were calculated using standard statistical mechanics equations for an ideal gas. All vibrations are considered strictly harmonic. Except for H_2, the rotational and translational contributions to the thermodynamic functions of CoP and motifs A, B, and C represent a small fraction, and almost compensate between the products and reactants of the reaction. In contrast, the translational entropy of H_2 is found to be significant and is actually the dominant entropic contribution in the reaction.

2.2.3. Exchange coupling constant J. We have evaluated the exchange coupling constant J for the fused CoP molecules for motifs A, B, and C (figure 5) using both broken-symmetry (BS) formalism and CASSCF/NEVPT2 calculations. The J constant parametrizes the interaction between the two spin $S = 1/2$ of the Co(II) centers, through the Heisenberg–Dirac–van Vleck Hamiltonian, with $\hat{H} = -J\hat{S_1}\hat{S_2}$. We use the Yamaguchi BS formalism [42], where the J constant can be evaluated from the energy difference between the high-spin (HS) solution (a triplet in this case) and the BS solution, with $M_s = 0$:

$$J = -2\frac{E_{\mathrm{HS}} - E_{\mathrm{BS}}}{\langle S^2\rangle_{\mathrm{HS}} - \langle S^2\rangle_{\mathrm{BS}}}. \quad (3)$$

In the case of CASSCF/NEVPT2, an active space containing 14 electrons distributed in ten $3d$ Co orbitals has been employed and J is obtained from the energy difference between the singlet and triplet states: $J = E_S - E_T$.

2.2.4. CoP on Au(111). The geometry, electronic structure, and relative energy of the CoP monomers and dimers on Au(111) surface were determined from periodic DFT based calculations in the framework of the Vienna *ab − initio* simulation package [43–46]. The PBE functional [47] was used. An effective Hubbard term U_{eff} of 1.9 eV is employed to describe the localized 3*d* orbitals of Co centers using Dudarev's approach ($U = 2.1$ eV, $J = 0.2$ eV) [48]. This U_{eff} value was shown to correctly describe the electronic $S = 1/2$ ground state of CoP and reproduce the energy separation between the ground doublet and excited quartet state obtained by Rovira *et al* [49] combining periodic DFT calculations with Becke–Perdew functional and Car–Parrinello molecular dynamics method for the optimization of the atomic structures. The van der Waals dispersion effects were included by the D2 method of Grimme *et al* [40]. The projector-augmented wave [50, 51] potentials were employed for all the atoms. To model the gold surface, first the parameters of the Au bulk were optimized ($a = b = c = 2.896$ Å). These calculated values are used to build the Au(111) surface and maintained fixed during the atomic position relaxation. The Au(111) surface is modelled by a three-layer slab with 270 atoms (25.08 Å×26.06 Å). A vacuum of 16.7 Å is added in the z direction to avoid the interaction between the slabs. The atoms of the lowest layer are kept fixed at bulk optimized positions, while the atoms of the two upper layers are relaxed, as well as the deposited CoP molecules. All the calculations refer to the Γ-point of Brillouin's zone, with an energy cut-off of 500 eV for the plane-wave basis set representing the valence electrons. Electronic relaxation was performed until the change in the total energy between two consecutive steps is smaller than 10^{-6} eV and the ionic relaxation was performed until the Hellmann–Feynman forces were lower than 0.02 eV Å^{-1}. To evaluate the charge transfer between gold surface and the deposited CoP molecule, a Bader charge analysis was performed, based on the electronic density provided by periodic calculations. The code developed by Henkelman and coworkers was employed [52].

3. Results and discussion

The Co^{2+} ion within CoP has a d^7 configuration with a square-planar ligand field. The complex is expected to exhibit a $S = 1/2$ ground state in the gas phase according to first-principle calculations [49], although recent studies evidenced difficulties in obtaining the correct ground state [53, 54]. It should be noted that, while Co tetraphenyl-porphyrin and substituted version thereof [55] were largely investigated on surfaces [56–59], CoP has attracted less attention. Schwarz *et al* [60] reported a detailed structural investigation, combining STM, x-ray photoelectron spetroscopy, x-ray standing wave measurements, and DFT calculations of CoP on Cu(111). The authors found that the axis formed by the two diagonally oriented pyrrole groups, with the cobalt atom positioned in between, aligns with a densely packed direction of the surface. In contrast, the remaining two pyrrole groups are tilted away from the surface. This structural asymmetry, induced by the adsorption of the complex on the Cu(111) surface, results in the molecules exhibiting a moderately saddle-shaped appearance in the STM images [60].

Figure 1(B) shows an overview STM image of CoP on Au(111) after sublimation on a sample held at room temperature (no post annealing). A close view of a few CoP molecules is shown in figure 1(C) along with a height profile across a molecule in figure 1(D). CoP on Au(111) exhibits a square shape with a lateral extent of approximately 1.5 nm and an apparent height of ≈ 100 pm at a sample voltage of −2 V. In particular, in contrast to CoP on Cu(111) [60], the complex does not appear to adopt a detectable saddle-shape conformation. We also note that we do not resolve any modulation of the apparent height that would be caused by the underlying herringbone reconstruction of the Au(111) surface. Furthermore, we do not observe any notable differences in the molecular appearance or behaviour depending on whether the molecules are adsorbed on *fcc* or *hcp* regions. This suggests that the specific adsorption site has only a limited influence on the molecular properties, in line with our on-surface DFT calculations (discussed below).

The overview image (figure 1(B)) further shows that the molecules occupy the whole surface and do not aggregate into dense, close-packed islands, as observed for other metallo-porphyrin complexes [61, 62]. Instead, the molecules appear to maximize their distance to their neighbors, with very few occurrence of 'contacted' neighboring molecules. To further analyze the molecular arrangement, we measured the distances between each molecule and its four-nearest neighbors. The resulting histogram is shown in figure 1(E). The average intermolecular distance is 1.78 nm, with a standard deviation of $\sigma = 0.34$ nm. This average distance is significantly larger than the calculated Co–Co distance for homocoupled molecules ($[0.83, 0.91]$ nm, see discussion below). The observation of a preferred intermolecular distance, rather than an equiprobable intermolecular-distance distribution, indicates an interaction between molecules. As the intermolecular distance is significantly larger than that of closed-packed molecules, the interaction is repulsive [63–65]. The dispersion of CoP molecules on the surface of Au(111) is consistent with previous findings of H_2P molecules on Au(111) [21, 23] and Ag(111) [60, 66]. The peculiar adsorption of the molecules was attributed to electrostatic repulsion caused by a partial charging of the molecules on the surface [66].

This electrostatic repulsion between the molecules is further supported by gas-phase DFT calculations. Figures 2 show three dimer configurations with relaxed atomic coordinates, indicating that these arrangements are stable and correspond to energy minima. Notably, these dimeric structures (Dimers 1 to 3 in figure 2) are energetically favoured by 41, 59, and 62 meV over separated monomers. The respective Co–Co distances for these dimers are 1.256, 1.119, and 1.171 nm, i.e. Co–Co distances shorter than those observed for CoP molecules deposited on Au(111). These gas-phase calculations, which inherently assume the molecules are *charge neutral*, suggest that close packing is preferred, with side-by-side configurations (figure 2) being particularly favourable. This result is an indication that CoP molecules become charged upon adsorption.

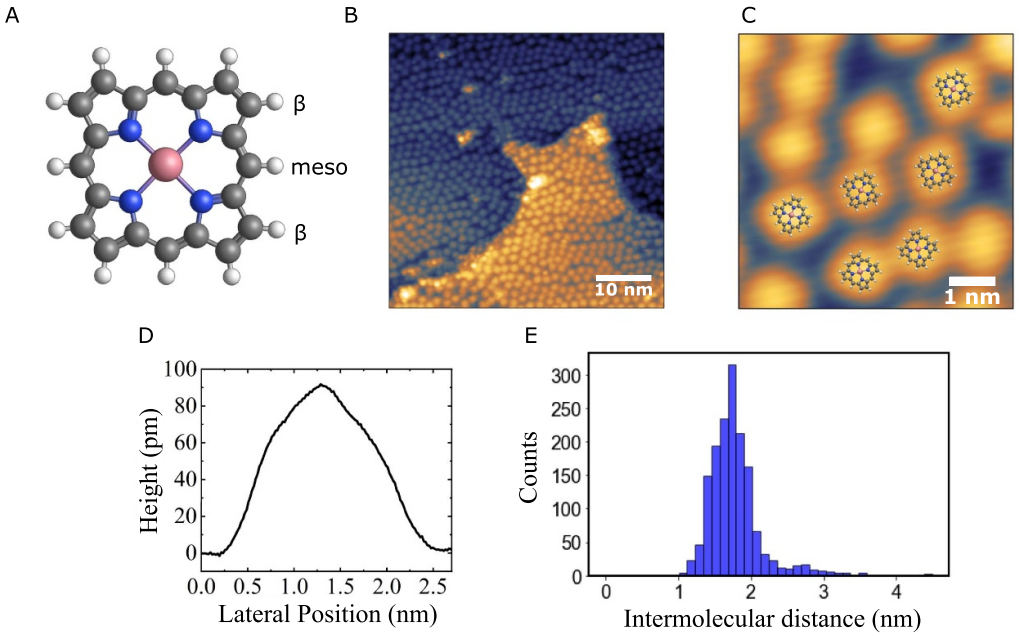

Figure 1. (A) Schematic representation of the Co porphyrin molecule indicating the two primary peripheric bonding sites: β and *meso*. The color code for atoms is as follows: reddish for cobalt (Co), dark gray for carbon, blue for nitrogen, and white for hydrogen. (B) STM image (-2 V, 100 pA) of CoP molecules on a Au(111) surface. Note that the image spans over two Au(111) terraces (orangish and blueish surfaces). Defining 1 ML as the maximum H_2P coverage on Au(111)—corresponding to a molecular density of 0.84 molecule/nm^2 [23]—the sample has a coverage of approximately 0.3 ML. (C) Zoomed STM image (-2 V, 100 pA) of CoP molecules. A model of a CoP molecule is overlaid on a few of them. (D) Apparent-height profile across a single CoP molecule. (E) Histogram of the intermolecular distance extracted from (B).

To unambiguously confirm that the separation between monomers is driven by electrostatic interactions, we performed DFT calculations of the molecules adsorbed on the surface. Our calculations reveal five distinct adsorption configurations, corresponding to four possible adsorption sites of the central Co ion relative to the Au(111) surface—*fcc*, *hcp*, bridge, and top—and two possible azimuthal orientations for the molecule with a bridge adsorption site (figure 3). The energy differences between these configurations are relatively small, all within a range of 80 meV. In all cases, the Co center exhibits a local spin of $S = 1/2$, while the total magnetization of the molecule is approximately 0.8 μ_B. This indicates a slight quenching of the Co spin, likely due to interactions with the bridging nitrogen atoms of the porphyrin ligand. A Bader charge analysis indicates that the molecule becomes positively charged upon adsorption, with a net charge of approximately $+0.35$ e. Using simple point-charge electrostatic considerations, two charges of $q = 0.35$ elementary charges separated by a distance of 1.2 nm—corresponding to the equilibrium distance of the non-fused dimers (figure 2)—result in an increase in potential energy of approximately 150 meV. This potential energy is roughly two to three times the interaction energy in the gas phase (figure 2), further supporting the conclusion that the dispersion of monomers on the surface is predominantly driven by electrostatic interactions.

Annealing of metal-free porphyrin molecules on Au(111) and Ag(111) was shown to trigger the covalent bonding between the molecules on the surfaces along with desorption of monomers [21, 23]. Annealing of CoP on Au(111) to $\approx 350^\circ$ C results in the desorption of approximately 30% of the CoP molecules from the surface. The remaining molecules form extended dendrite-like aggregates, several tens of nanometre wide, as shown in the STM image in figures 4(A) and (B). This linear assembly and disordered behavior are similar to previous large oligomers formation observed with the metal-free porphyrin on Au(111) [23]. As such the homocoupling of CoP on Au(111) is supposedly semblable to that of metal-free base porphyrin on Au(111).

The formation of large molecular aggregates also influences the appearance of individual molecules. Before annealing, the molecules exhibit a squarish shape with a relatively uniform apparent height. After annealing, their appearance changes significantly: the centre of the molecule—corresponding to the position of the Co ion—appears much brighter, as shown in the zoomed STM image in figure 4(D). This change in appearance may have two potential origins: (i) Bonding to neighbouring complexes may alter the molecule's conformation, for example, from a minor saddle shape to a more planar configuration. (ii) A modification of the electronic structure. To directly probe (ii), we measured the differential-conductance spectrum atop a molecule within an aggregate. The spectrum is essentially featureless within the energy range $[-2.5, 2.5]$ eV (figure 4(C)). If electronic states exist within this range, they are very broad, which suggests strong electronic coupling of the molecule to the substrate. Indirect evidence regarding (ii) comes from comparing the data before and after annealing. Before annealing, the isolated character of the molecules is associated with charging

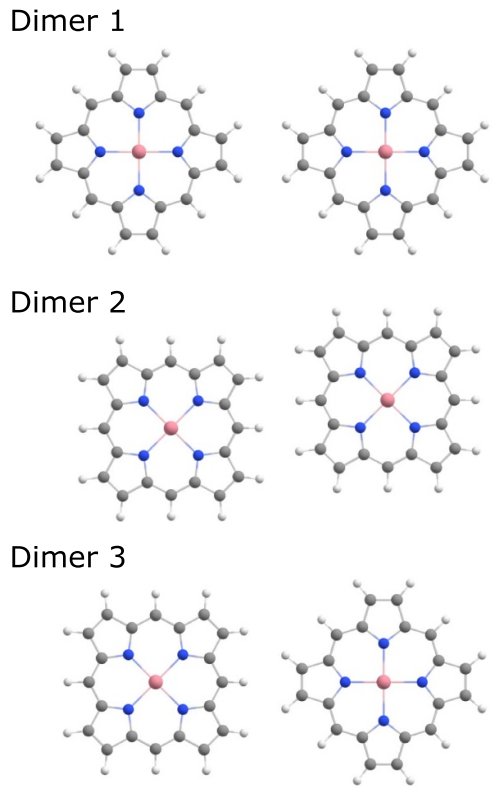

Figure 2. Calculated structures of three configurations of dimers in the gas phase.

(resulting from charge transfer between the molecule and the substrate), causing intermolecular electrostatic repulsion. After annealing, the formation of aggregates evidences that this repulsion has been overcome, likely due to a reduction in the molecule–substrate charge transfer. These observations suggest different charge states for the molecules in their isolated and aggregated forms, which translates into their distinct appearances in the STM topographs. This point will be confirmed below with DFT calculations of molecular dimers on Au(111).

It is worth noting that the molecular dendrites extend both across and along the underlying herringbone reconstruction of the Au(111) surface (figure 4(A)). In particular, there is no apparent correlation between the orientation of the dendrites and the reconstruction lines—confirmed by a statistical analysis shown in appendix A—, indicating that the reconstruction has a negligible influence on the CoP complexes.

We conducted a statistical analysis of the STM images after annealing to further characterise the molecular aggregates. To simplify the analysis, we considered intermolecular distances below 1.38 nm—corresponding to the onset of the intermolecular-distance distribution prior to annealing—as indicative of homocoupling. For 499 molecules, we determined the number of nearest neighbours with intermolecular distances below the 1.38 nm threshold and presented the results as a histogram in figure 4(E). The largest fraction of molecules (37%) has two neighbours, confirming a preference for chain-like growth. Approximately 29% of the molecules have three neighbours, resulting in bifurcations within the chains and contributing to the overall impression of unorganised aggregates.

The distribution of intermolecular distances among coupled molecules—those with distances below 1.38 nm—is shown in figure 4(F). The average molecular distance is 1 nm, with a standard deviation of ≈ 0.2 nm. This relatively large variation suggests the presence of multiple types of bonding between molecules, each characterised by different intermolecular distances.

Figure 5 presents the structures, inferred from gas-phase DFT calculations, of three motifs observed in the experiment. In Motif A (figure 5(A)), two CoP complexes are positioned side by side, forming three covalent bonds: two involving β–β sites and one involving two *meso* sites. This configuration results in the formation of two six-membered carbon rings. The gas-phase structure of this dimer is flat, which likely facilitates adsorption on a surface by enhancing van der Waals interactions between the molecules and the substrate [23, 67]. A modification of Motif A, where one molecule is displaced perpendicular to the initial Co–Co axis, produces Motif B (figure 5(B)). In this motif, the lateral overlap between the molecules is reduced, resulting in only two covalent bonds compared to the three present in Motif A. The connection between the two monomers forms a single six-membered carbon ring. A side view of the dimer (bottom panel in figure 5(B) reveals a ruffled conformation, with a modulation in height across the dimer. In Motif C (figure 5(C)), one molecule is azimuthally rotated by 45° relative to its neighbor. This arrangement forms two additional covalent bonds between the monomers, resulting in a five-membered carbon ring. Similar to Motif B, the dimer exhibits significant distortion in the gas phase, which as shown below is largely alleviated upon adsorption on Au(111). It should be noted that Seufert *et al* [23] identified all these three motif, as well as a fourth motif, of a metal-free porphyrin dimer on Au(111). The latter motif is characterized by a single covalent bond between the monomers at the β sites. While we did not unambiguously observe such a bonding in our experiments, it is important to emphasize that the insufficient resolution of our images prevented us from identifying *all* connections between the CoP complexes.

The bonding between the molecules was inferred from high-resolution STM images. Relaxed dimer structures of motifs A, B, and C, upon adsorption on the surface, were scaled and overlaid onto the STM image shown in figure 6, and these motifs were encircled in red, green, and white, respectively. This analysis of the bonding nature between neighbouring molecules was conducted for $\approx 80\%$ of the molecules, where the STM image provided sufficient clarity for unambiguous identification. The experimentally inferred average Co–Co distances are 8.9, 9.4, and 9.5 Å for motifs A, B, and C, respectively. These values are in relatively good agreement with the calculated distances of 8.3, 8.6, and 9.1 Å. The experimentally observed trend of increasing Co–Co distances from motif A to motif C is consistent with the calculated trend, with deviations remaining below 10%. Table 1 summarises the experimentally extracted data on the bonding between molecules, along with the calculated quantities for the three

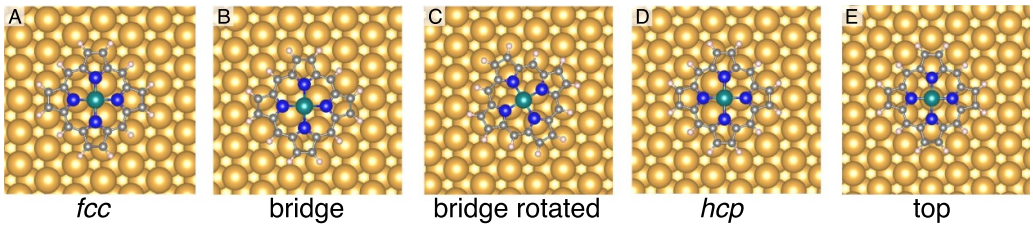

Figure 3. Calculated structures of a CoP monomer on Au(111). The adsorption sites of the Co ion are (A) *fcc*, (B) bridge, (C) bridge, (D) *hcp*, and (E) top. Note that two stable azimuthal configurations are found for the bridge adsorption site. The relative energies of these configurations are (A) 0, (B) 50, (C) 9, (D) 15, and (E) 81 meV, respectively.

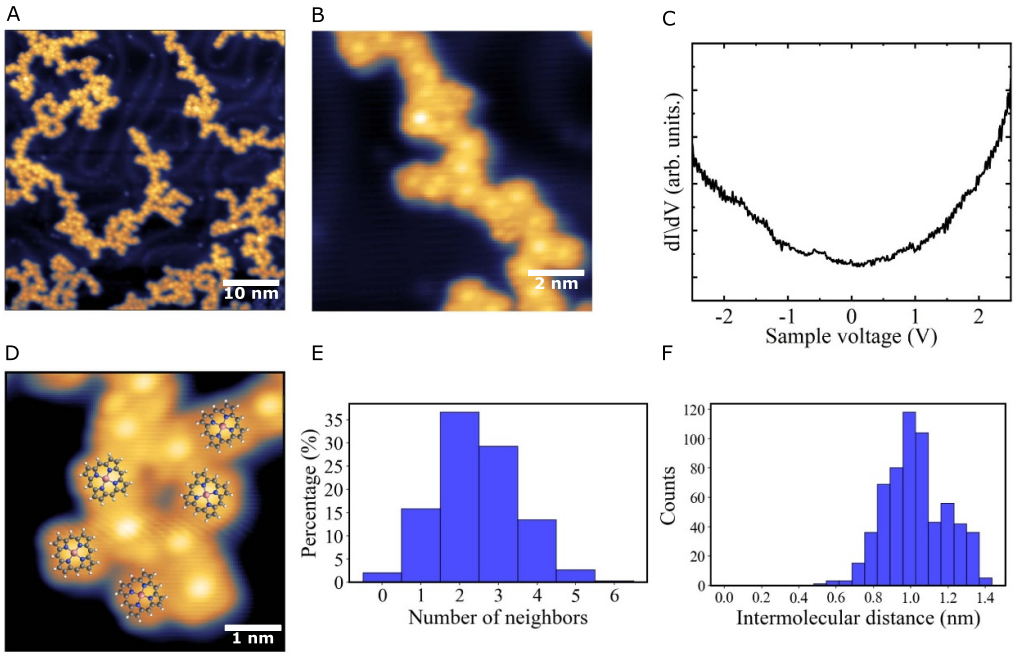

Figure 4. (A) STM image (−1 V, 200 pA) of CoP complexes, after annealing of the sample, exhibiting disordered chains of CoP molecules. (B) Zoomed STM image ($10 \times 10\,\mathrm{nm}^2$, −1 V, 200 pA) showing a closer view of CoP molecules. (C) Differential-conductance spectrum of a CoP molecule within a chain, essentially featureless. (D) Zoomed STM topograph of CoP molecules on Au(111), with overlaid CoP model, exhibiting a protrusion in their center. (E) Distribution of the number of neighboring CoP molecules within a distance of 1.38 nm, for each molecule in the chain, extracted from 499 molecules in the image in (A). (F) Histogram of the intermolecular distances, extracted from the STM image in (A), of molecules separated by less than 1.38 nm. The average distance is 1 nm with a standard deviation of 0.2 nm.

motifs. The occurrence of dimeric bonding motifs A, B, and C is 33%, 15%, and 52%, respectively. The higher occurrence of motif C aligns with earlier studies on porphyrin molecules adsorbed on Au(111) [23].

To estimate the likelihood of different dimeric bonding configurations forming during the annealing process, we calculated the Gibbs free energy in the gas phase for the formation reactions of the various motifs using:

$$\Delta G = G_{\mathrm{M}_x} + N_{\mathrm{H}_2} \cdot G_{\mathrm{H}_2} - N_{\mathrm{P}} \cdot G_{\mathrm{P}}, \tag{4}$$

where N_{P} is the number of fusing CoP molecules (2 for dimers), N_{H_2} the number of H_2 molecules released during the reaction. G_{M_x}, G_{H_2}, and G_{P} describe the Gibbs free energy of the Motif x, hydrogen, and CoP molecules, respectively. The Gibbs free energy values for the formation reactions of motifs A, B, and C at temperatures of 298.15 K and 623.15 K for atmospheric (10^5 Pa) pressure and ultrahigh vacuum (10^{-8} Pa) are summarised in table 1 (see Methods for computational details). At $T = 623$ K and $P = 10^{-8}$ Pa, we find Gibbs free energies of −4.19, −1.37, and −0.48 eV for the reaction formation of dimers A, B, and C, respectively.

The pressure, and more specifically the ultrahigh vacuum, appears to play a crucial role in the homocoupling reaction. While only the formation of motif A is thermodynamically favourable at atmospheric pressure—reflected by a negative Gibbs free energy—the dimerization leading to all considered motifs becomes feasible under ultrahigh vacuum conditions. As noted in references [23, 68], the evaporation of H_2 in the ultrahigh vacuum introduces an additional entropic contribution, reducing the free energy by approximately 2.5 eV.

Nonetheless, Motif C is predominantly observed, even though Motif A is the most thermodynamically stable configuration in the gas phase. This discrepancy may be attributed to the adsorption of the dimer onto the surface, which leads

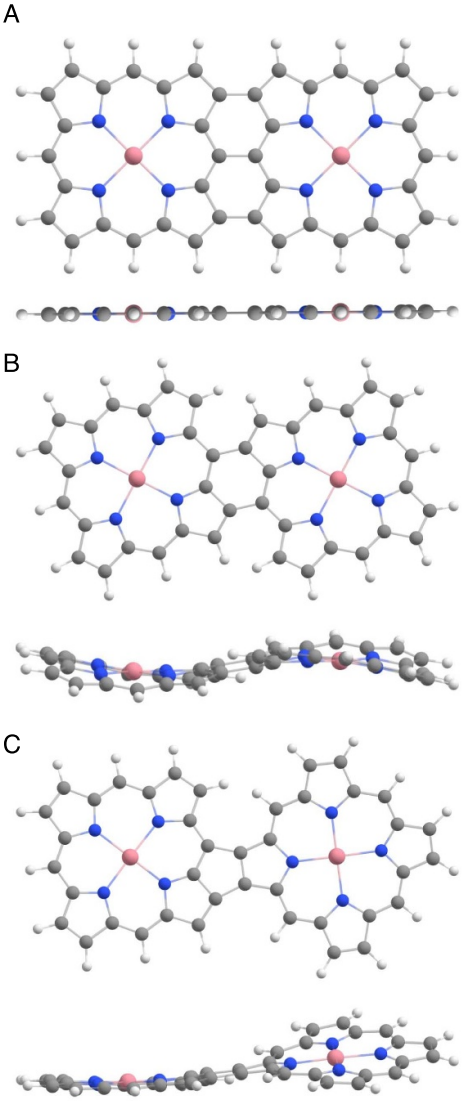

Figure 5. Calculated gas-phase structures of three CoP dimers identified in the STM images. (A) Side-by-side arrangement of the molecules with three covalents bonds (two at the β sites and one *meso* site) viewed (top) from the top and (bottom) from the side. The connection between the complexes form two six-membered rings. The dimer is flat. (B) Another side-by-side configuration of the complexes. However, because of a relative shift between the molecules, only two covalent bonds are formed (two β-*meso* bonds). The bonding form a six-membered ring and the corresponding dimer has a ruffled shape (in the gas phase). (C) Arrangement where the molecules have different relative azimuthal orientations. The two covalent bonds between the monomers (β–β, β-*meso*) form a five-membered ring. The dimer is not flat but exhibits a distortion.

to its planarization and could alter the relative stabilities of the motifs. To explore this aspect, we performed DFT calculations for the three dimer motifs adsorbed on Au(111). The resulting structures are shown in figure 7, and the corresponding properties are listed in table 2. Upon dimerization, the Co ions of the two monomers largely retain their local spins of $S = 1/2$. In Motif A, the Co ions adopt bridge and *fcc* adsorption sites, whereas in Motifs B and C, only bridge sites are observed.

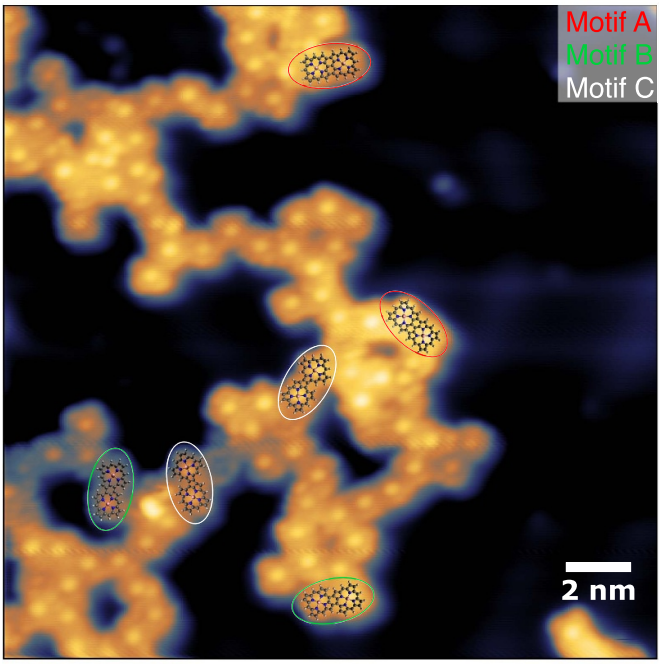

Figure 6. STM image (−1 V, 200 pA) of CoP on Au(111) after homocoupling reaction. Scaled structure of the dimers, as inferred from the on-surface DFT calculations, are overlaid on the image. The color code encircling the dimers describes the motif following the legend shown in the upper-right of the image.

The calculated Co–Co distances for the adsorbed dimers are 8.36, 8.80, and 9.14 Å for Motifs A, B, and C, respectively. These values differ by less than 3% from those calculated in the gas phase, indicating minimal structural extension or contraction upon adsorption. As anticipated, the dimers lie relatively flat on the surface. The largest molecular corrugation—defined as the height difference between the lowest and highest atoms within the molecule—is found for Motif B, with a value of only 0.65 Å.

The dimers retain a net positive charge of approximately 0.4–0.5 elementary charges per dimer. For comparison, the monomer exhibits a charge of about 0.35 e, implying a 55%–65% reduction in metal-to-molecule charge transfer upon dimerization. The spatial distribution of the charge is discussed in appendix B. By extension, one may speculate that the charge transfer continues to decrease as the number of molecules within the aggregate increases.

From an energetic standpoint, the on-surface DFT calculations largely confirm the gas-phase results: Motif A remains the most stable configuration, followed by Motif B and Motif C, which are 0.11 eV and 0.93 eV higher in energy, respectively. This supports the notion that the observed dimer formation is governed by kinetic limitations, as convincingly argued in reference [23]. The fusing of two CoP molecules involves the formation of two or three C–C covalent bonds, depending on the motif. These bonds most likely form sequentially, with the initial β–β bond being the most favourable, as discussed in reference [23]. Motif B—which involves two β–*meso* bonds—would then be the kinetically least favourable

Table 1. Motifs of gas-phase CoP dimers. Occurence, proportion, experimental and calculated distance between the Co centers, Gibbs free energy calculated at 298.15 and 623.15 K, and calculated height corrugation of the different dimers. The uncertainty in the experimental Co–Co distance is given by the standard deviation. The height corrugation $d_{\text{corr.}}$ is defined as the largest height difference between atoms of the same dimer.

	Experiments			Calculations					
Motif	Occ.	Prop. (%)	$d_{\text{Co–Co}}$ (Å)	$d_{\text{Co–Co}}$ (Å)	ΔG (eV) $T = 298$ K $P = 10^5$ Pa	ΔG (eV) $T = 298$ K $P = 10^{-8}$ Pa	ΔG (eV) $T = 623$ K $P = 10^5$ Pa	ΔG (eV) $T = 623$ K $P = 10^{-8}$ Pa	$d_{\text{corr.}}$ (Å)
A	16	33	8.9 ± 0.2	8.3	−0.56	−2.08	−1.01	−4.19	0.23
B	7	15	9.4 ± 0.2	8.6	0.14	−0.63	0.11	−1.37	1.97
C	25	52	9.5 ± 0.2	9.1	1.08	0.30	1.01	−0.48	2.84

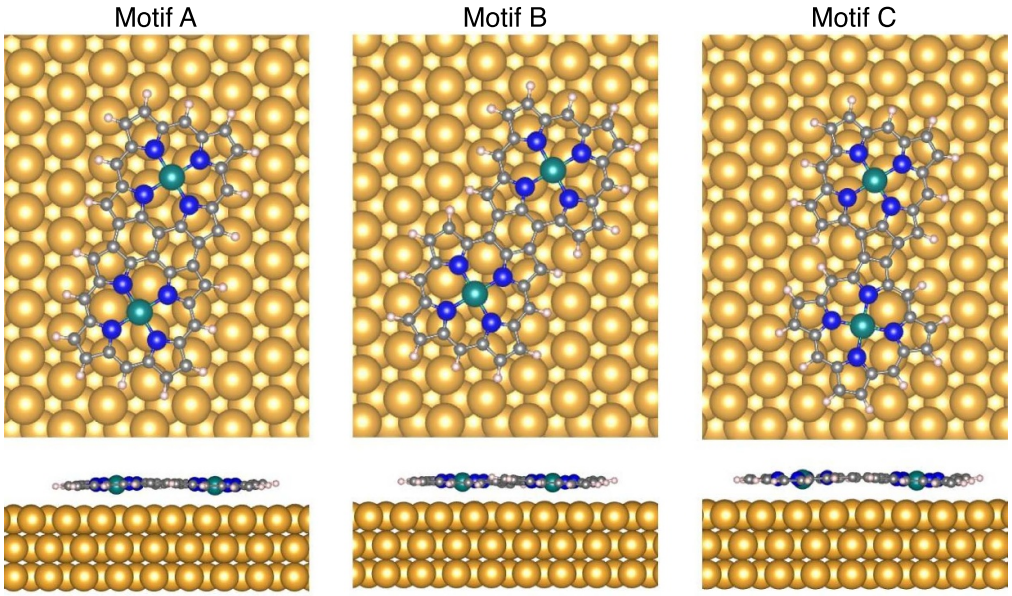

Figure 7. Top-view (upper panels) and side-view (lower panels) representations of CoP dimers adsorbed on Au(111), as obtained from our DFT calculations. The three configurations—A, B, and C—correspond to the motifs shown in figure 5. Detailed calculated properties of these dimers are provided in table 2.

Table 2. Calculated properties of the dimers adsorbed on Au(111). ΔE indicates the difference in the formation energy of each motif from gas-phase CoP monomer and the surface: 2 CoP(g) + surface → fused-CoP + nH$_2$, with $n = 3$ for motif A, and $n = 2$ for motifs B and C. Note that a hydrogen molecule was added to Motif A to ensure a comparable number of atoms across the different motifs. The definitions of $d_{\text{Co–Co}}$ and $d_{\text{corr.}}$ are consistent with those used in table 1.

Motif	ΔE (eV)	Bader charge (e)	$d_{\text{Co–Co}}$ (Å)	$d_{\text{corr.}}$ (Å)
A + H$_2$	0.00	+0.42	8.36	0.38
B	0.11	+0.47	8.80	0.65
C	0.93	+0.48	9.14	0.50

structure, consistent with experimental observations. Another important factor in the kinetic description is the relative pre-alignment of the molecules.

We now consider the magnetic interaction between the $S = 1/2$ spins of the Co ions in fused CoP molecules (Motif A), described by the Heisenberg-Dirac-van Vleck Hamiltonian:

$$\hat{H} = -J\hat{S_1}\hat{S_2}, \tag{5}$$

where $\hat{S_i}$ is the spin operator for ion i, and J is the exchange constant that characterises the interaction (see Methods for calculation details). The resulting exchange constants determined from BS gas-phase DFT calculations were weakly antiferromagnetic, with J values of −2.1, −0.8 and −0.2 meV for motif A, B and C, respectively. CASSCF/NEVPT2 calculations on motif A confirms that the coupling is very weak ($J = -0.06\,\text{cm}^{-1} = 7 \times 10^{-3}$ meV, in the limit of the precision of these calculations). The exchange coupling is antiferromagnetic and too weak to be resolved via spin-flip spectroscopy with our instrumentation, which has an energy resolution on the order of 2 meV. The overall weak magnetic coupling between the centres can be attributed to the spin of each molecule being primarily localised in a single-occupied $3d_{z^2}$ orbital, with minimal delocalisation into the sigma orbitals of the bridging moieties.

Despite the low magnetic coupling, our study evidence that the surface-assisted fusing of porphyrin molecules can be extended to metal porphyrin complexes. This strategy can be

further employed with other magnetic metal centers, potentially exhibiting much larger magnetic coupling.

4. Conclusion

In this study, we investigated the thermally induced covalent coupling of CoP molecules on an Au(111) surface. At room temperature, CoP molecules deposited on the surface remained isolated due to electrostatic repulsion. However, annealing the substrate promoted the aggregation of molecules into chain-like structures, with evidence of covalent bonding confirmed by DFT calculations. Our findings identified three primary bonding motifs formed during the homocoupling process, characterised by distinct Co–Co distances and structural conformations. Gas-phase calculations for a CoP dimer revealed a weak antiferromagnetic coupling between the spin-$1/2$ of the Co ions, though the interaction was too small to be experimentally detected with the available instrumentation. This study presents a promising approach for synthesising multinuclear complexes with magnetically coupled spins directly on surfaces, without necessitating specific substitutions of the complexes. Such advancements offer significant potential for applications in molecular spintronics.

Data availability statement

The data cannot be made publicly available upon publication because the cost of preparing, depositing and hosting the data would be prohibitive within the terms of this research project. The data that support the findings of this study are available upon reasonable request from the authors.

Acknowledgments

This work was funded by the Deutsche Forschungsgemeinschaft (DFG, German Research Foundation) Project No. 278162697-SFB 1242. C J C, R S A and N M P acknowledge the financial support through grant PID2021-127674NB-I00 funded by MICIU/AEI/10.13039/501100011033/FEDER/UE. The technical support of the Supercomputing Team of the Centro Informático Científico de Andalucía (CICA) and Cénits-COMPUTAEX (Extremadura, Spain) is also acknowledged.

Conflict of interest

The authors declare that they have no conflicts of interest.

Appendix A. Orientation of the molecular aggregates

The molecular aggregates observed in figure 4(A) appear to be randomly oriented on the surface. To quantify this impression, we measured the orientation angles of 251 dendritic structures relative to the $\langle 1\bar{1}0\rangle$ crystallographic direction of the Au(111) substrate. The resulting histogram is shown in figure A1. No strongly preferred orientation is observed; rather, the distribution appears uniform, with minor fluctuations attributable to the limited statistical sample size.

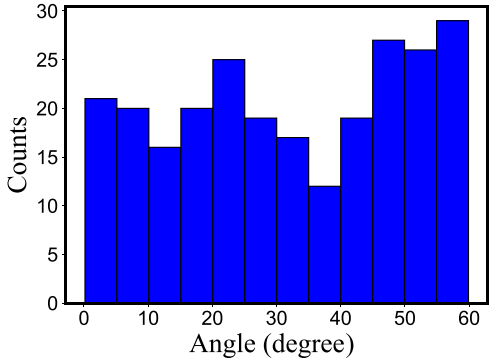

Figure A1. Orientation distribution of the molecular aggregates relative to the $\langle 1\bar{1}0\rangle$ crystallographic direction of the Au(111) substrate.

Appendix B. Charge redistribution upon adsorption

Figure B1 shows the plots of the difference of the electronic density, $\Delta\rho$, between the deposited molecules and the superposition of the electronic density of the molecule and the surface, $\Delta\rho = \rho_{\text{total}} - (\rho_{\text{molecule}} + \rho_{\text{substrate}})$. Blue (yellow) surfaces represent regions where the electronic density decreases (increases) upon adsorption. Hence, the molecules are positively charged (predominance of blue surfaces) once deposited, in line with the Bader-charge analysis reported in table 2.

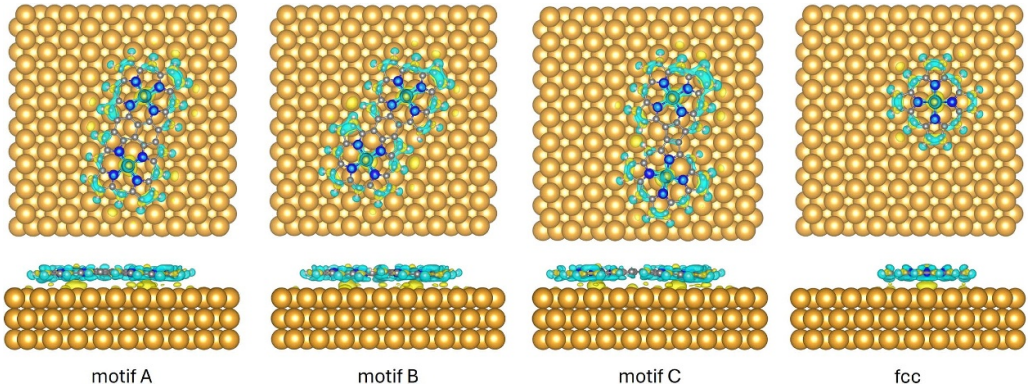

Figure B1. Calculated structures of the dimers and *fcc* monomer on Au(111) along with the change in electronic density upon adsorption. Blue areas indicate a decreased electronic density such that the corresponding regions are positively charged.

ORCID iDs

Mehdi Bouatou https://orcid.org/0009-0006-0129-6909
Nicolás Montenegro-Pohlhammer https://orcid.org/0000-0003-3574-2955
Rocío Sánchez-de-Armas https://orcid.org/0000-0002-2384-4893
Carl Barthel https://orcid.org/0009-0000-4967-8646
Carmen J Calzado https://orcid.org/0000-0003-3841-7330
Manuel Gruber https://orcid.org/0000-0002-8353-4651

References

[1] Otero R, Gallego J M, de Parga A L V, Martín N and Miranda R 2011 *Adv. Mater.* **23** 5148–76
[2] Jasper-Tönnies T, Gruber M, Ulrich S, Herges R and Berndt R 2020 *Angew. Chem.* **132** 7074–83
[3] Cinchetti M, Dediu V A and Hueso L E 2017 *Nat. Mater.* **16** 507–15
[4] Coronado E 2019 *Nat. Rev. Mater.* **5** 87–104
[5] Grill L, Dyer M, Lafferentz L, Persson M, Peters M V and Hecht S 2007 *Nat. Nanotechnol.* **2** 687–91
[6] Houtsma R K, van Zuilen J and Stöhr M 2024 *Adv. Mater. Interfaces* **11** 2300728
[7] Franc G and Gourdon A 2011 *Phys. Chem. Chem. Phys.* **13** 14283–92
[8] Steiner C, Fromm L, Gebhardt J, Liu Y, Heidenreich A, Hammer N, Görling A, Kivala M and Maier S 2021 *Nanoscale* **13** 9798–807
[9] Schulz F *et al* 2017 *J. Phys. Chem. C* **121** 2896–904
[10] Dai J, Fan Q, Wang T, Kuttner J, Hilt G, Gottfried J M and Zhu J 2016 *Phys. Chem. Chem. Phys.* **18** 20627–34
[11] Eichhorn J, Nieckarz D, Ochs O, Samanta D, Schmittel M, Szabelski P J and Lackinger M 2014 *ACS Nano* **8** 7880–9
[12] Held P A, Fuchs H and Studer A 2017 *Chem. Eur. J.* **23** 5874–92
[13] Herrera-Reinoza N, Mowbray D J, Pérez Paz A, Ceccatto Dos Santos A, De Campos Ferreira R C and De Siervo A 2025 *J. Phys. Chem. C* (https://doi.org/10.1021/acs.jpcc.4c08308)
[14] Hla S W, Bartels L, Meyer G and Rieder K H 2000 *Phys. Rev. Lett.* **85** 2777–80
[15] Schuler B, Fatayer S, Mohn F, Moll N, Pavliček N, Meyer G, Peña D and Gross L 2016 *Nat. Chem.* **8** 220–4
[16] Sun W, Wang H, Liang Z, Huang C, Ma J, Xie L and Song F 2025 *J. Phys. Chem. C* **129** 7771–9
[17] Gottfried J M 2015 *Surf. Sci. Rep.* **70** 259–379
[18] Clair S and de Oteyza D G 2019 *Chem. Rev.* **119** 4717–76
[19] Judd C J, Kondratuk D V, Anderson H L and Saywell A 2019 *Sci. Rep.* **9** 9352
[20] Chen C, Joshi T, Li H, Chavez A D, Pedramrazi Z, Liu P N, Li H, Dichtel W R, Bredas J L and Crommie M F 2018 *ACS Nano* **12** 385–91
[21] Wiengarten A *et al* 2014 *J. Am. Chem. Soc.* **136** 9346–54
[22] He Y, Garnica M, Bischoff F, Ducke J, Bocquet M L, Batzill M, Auwärter W and Barth J V 2017 *Nat. Chem.* **9** 33–38
[23] Seufert K, McBride F, Jaekel S, Wit B, Haq S, Steiner A, Poli P, Persson M, Raval R and Grill L 2019 *J. Phys. Chem. C* **123** 16690–8
[24] Rascon E C, Riss A, Matěj A, Wiengarten A, Mutombo P, Soler D, Jelinek P and Auwärter W 2023 *J. Am. Chem. Soc.* **145** 967–77
[25] Kahle S *et al* 2012 *Nano Lett.* **12** 518–21
[26] Burgess J A J *et al* 2015 *Nat. Commun.* **6** 8216
[27] Knaak T, Gruber M, Lindström C, Bocquet M L, Heck J and Berndt R 2017 *Nano Lett.* **17** 7146
[28] Knaak T, Gruber M, Puhl S, Benner F, Escribano A, Heck J and Berndt R 2017 *J. Phys. Chem. C* **121** 26777–84
[29] Li C *et al* 2023 *ACS Nano* **17** 10608–16
[30] Serri M, Wu W, Fleet L R, Harrison N M, Hirjibehedin C F, Kay C W M, Fisher A J, Aeppli G and Heutz S 2014 *Nat. Commun.* **5** 3079
[31] Gruber M *et al* 2015 *Nat. Mater.* **14** 981–4
[32] Boukari S *et al* 2018 *Nano Lett.* **18** 4659–63
[33] DiLullo A, Chang S H, Baadji N, Clark K, Klöckner J P, Prosenc M H, Sanvito S, Wiesendanger R, Hoffmann G and Hla S W 2012 *Nano Lett.* **12** 3174–9
[34] Bazarnik M, Bugenhagen B, Elsebach M, Sierda E, Frank A, Prosenc M H and Wiesendanger R 2016 *Nano Lett.* **16** 577–82
[35] Liu J, Gao Y, Wang T, Xue Q, Hua M, Wang Y, Huang L and Lin N 2020 *ACS Nano* **14** 11283–93
[36] De Oteyza D G and Frederiksen T 2022 *J. Phys.: Condens. Matter* **34** 443001
[37] Zhao C *et al* 2024 *Nat. Nanotechnol.* **19** 1789–95
[38] Zhao C *et al* 2025 *Nat. Mater.* **24** 722–7
[39] Sun K, Cao N, Silveira O J, Fumega A O, Hanindita F, Ito S, Lado J L, Liljeroth P, Foster A S and Kawai S 2025 *Sci. Adv.* **11** eads1641
[40] Grimme S, Antony J, Ehrlich S and Krieg H 2010 *J. Chem. Phys.* **132** 154104
[41] Neese F, Wennmohs F, Becker U and Riplinger C 2020 *J. Chem. Phys.* **152** 224108

[42] Soda T, Kitagawa Y, Onishi T, Takano Y, Shigeta Y, Nagao H, Yoshioka Y and Yamaguchi K 2000 *Chem. Phys. Lett.* **319** 223–30
[43] Kresse G and Hafner J 1993 *Phys. Rev. B* **47** 558–61
[44] Kresse G and Hafner J 1994 *Phys. Rev. B* **49** 14251–69
[45] Kresse G and Furthmüller J 1996 *Comput. Mater. Sci.* **6** 15–50
[46] Kresse G and Furthmüller J 1996 *Phys. Rev. B* **54** 11169–86
[47] Perdew J P, Burke K and Ernzerhof M 1996 *Phys. Rev. Lett.* **77** 3865–8
[48] Dudarev S L, Botton G A, Savrasov S Y, Humphreys C J and Sutton A P 1998 *Phys. Rev. B* **57** 1505–9
[49] Rovira C, Kunc K, Hutter J and Parrinello M 2001 *Inorg. Chem.* **40** 11–17
[50] Blöchl P E 1994 *Phys. Rev. B* **50** 17953–79
[51] Kresse G and Joubert D 1999 *Phys. Rev. B* **59** 1758–75
[52] Henkelman G, Arnaldsson A and Jónsson H 2006 *Comput. Mater. Sci.* **36** 354–60
[53] De Souza J R and De Moraes M M F, Aoto Y A and Homem-de Mello P 2020 *Phys. Chem. Chem. Phys.* **22** 23886–98
[54] Pogonin A E, Eroshin A V and Girichev G V 2025 *J. Mol. Struct.* **1329** 141419
[55] Meng X, Möller J, Menchón R E, Weismann A, Sánchez-Portal D, Garcia-Lekue A, Herges R and Berndt R 2024 *Nano Lett.* **24** 180–6
[56] Seufert K, Bocquet M L, Auwärter W, Weber-Bargioni A, Reichert J, Lorente N and Barth J V 2011 *Nat. Chem.* **3** 114–9
[57] Wäckerlin C, Siewert D, Jung T A and Ballav N 2013 *Phys. Chem. Chem. Phys.* **15** 16510–4
[58] Kim H, Son W j, Jang W J, Yoon J K, Han S and Kahng S J 2009 *Phys. Rev. B* **80** 245402
[59] Iancu V, Deshpande A and Hla S W 2006 *Nano Lett.* **6** 820–3
[60] Schwarz M *et al* 2018 *J. Phys. Chem. C* **122** 5452–61
[61] Yang Z Y and Durkan C 2010 *Surf. Sci.* **604** 660–5
[62] Wang W, Pang R, Kuang G, Shi X, Shang X, Liu P N and Lin N 2015 *Phys. Rev. B* **91** 045440
[63] Simpson S, Kunkel D A, Hooper J, Nitz J, Dowben P A, Routaboul L, Braunstein P, Doudin B, Enders A and Zurek E 2013 *J. Phys. Chem. C* **117** 16406–15
[64] Jin W, Liu Q, Dougherty D B, Cullen W G, Reutt-Robey J E, Weeks J and Robey S W 2015 *J. Chem. Phys.* **142** 101910
[65] Fernandez-Torrente I, Monturet S, Franke K J, Fraxedas J, Lorente N and Pascual J I 2007 *Phys. Rev. Lett.* **99** 176103
[66] Bischoff F *et al* 2013 *ACS Nano* **7** 3139–49
[67] Jasper-Tönnies T, Poltavsky I, Ulrich S, Moje T, Tkatchenko A, Herges R and Berndt R 2018 *J. Chem. Phys.* **149** 244705
[68] Floris A, Haq S, In't Veld M, Amabilino D B, Raval R and Kantorovich L 2016 *J. Am. Chem. Soc.* **138** 5837–47